HHS Public Access

Author manuscript

Acta Biomater. Author manuscript; available in PMC 2019 July 15.

Published in final edited form as:

Acta Biomater. 2018 July 15; 75: 463–471. doi:10.1016/j.actbio.2018.05.047.

Strontium-releasing fluorapatite glass-ceramic scaffolds: Structural characterization and *in vivo* performance

Isabelle Denry[a,b,*], **Ourania-Menti Goudouri**[a], **Douglas C. Fredericks**[c], **Adil Akkouch**[a], **Michael R. Acevedo**[d], and **Julie A. Holloway**[b]

[a]Iowa Institute for Oral Health Research, University of Iowa College of Dentistry, Iowa City, Iowa, United States

[b]Department of Prosthodontics, University of Iowa College of Dentistry, Iowa City, Iowa, United States

[c]Iowa Spine Research Laboratory, Department of Orthopaedic Surgery and Rehabilitation, University of Iowa Carver College of Medicine, Iowa City, Iowa, United States

[d]Department of Radiology, University of Iowa Roy J. and Lucille A. Carver College of Medicine, Iowa City, Iowa, United States

Abstract

There is increasing interest in biodegradable ceramic scaffolds for bone tissue engineering capable of *in situ* delivery of ionic species favoring bone formation. Strontium has been shown to be osteogenic, but strontium-containing drugs such as strontium ranelate, used in Europe for the treatment of osteoporosis, are now restricted due to clinical evidence of systemic effects. By doping fluorapatite-based glasses with strontium, we developed ceramic scaffolds with fully interconnected macroporosity and cell size similar to that of cancellous bone, that are also capable of releasing strontium. The crystallization behavior, investigated by XRD and SEM, revealed the formation of akermanite and fluorapatite at the surface of strontium-free glass-ceramic scaffolds, and strontium-substituted fluorapatite at the surface of the strontium-doped scaffolds. At 8 weeks after implantation in a rat calvarial critical size defect, scaffolds doped with the highest amount of strontium led to the highest mineral apposition rate. A significantly higher amount of newly-formed bone was found with the strontium-free glass-ceramic scaffold, and possibly linked to the presence of akermanite at the scaffold surface. We demonstrate by energy dispersive XRF analyses of skull sections that strontium was present in newly formed bone with the strontium-doped scaffolds, while a significant amount of fluorine was incorporated in newly formed bone, regardless of composition or crystallization state.

*Corresponding author at: The University of Iowa College of Dentistry, 801 Newton Road, Iowa City, IA 52242, United States. Isabelle-Denry@uiowa.edu (I. Denry).

Disclosures

All authors declare having no conflict of interest.

Keywords

Strontium; Fluorapatite; Akermanite; Scaffold; Osteogenesis

1. Introduction

Calcium phosphate-based ceramic scaffolds for bone graft substitutes have long been the focus of extensive research work [1,2]. Synthetic bone graft materials are attractive as they can be produced on a large scale. Polymeric synthetic scaffolds for bone replacement are easily produced by 3D printing or additives technologies and are therefore attractive, however, they lack essential mineral species and trace elements necessary for bone formation. Although these essential species can be included in a large palette of glass systems, only a limited compositional range exhibits adequate degradability and biosolubility. For example, bioglasses and glass-ceramics within the compositional range identified by Hench [3] are both bioactive and biodegradable. Calcium-phosphate based ceramic scaffolds therefore represent a logical choice for *in situ* delivery of calcium and phosphate during the early stages of mineralized bone formation [4–6]. In addition to calcium and phosphate, silicon, magnesium and a wide panel of metallic trace elements that are incorporated into bone structure have been shown to hold a key role in osteogenesis and angiogenesis, enhancing bone remodeling and repair processes [7]. Amongst these trace metallic elements, strontium has been extensively studied due to its similarity in charge and size with calcium, linked to its ability to substitute for calcium in the apatite structure [8]. It is now well established that strontium replaces calcium in osteoblast-mediated processes and enhances osteogenesis via osteoblast formation while preventing osteoclastic resorption. Moreover, strontium has been shown to enhance the differentiation of osteoblasts into osteocytes [9]. Osteocytes influence the function of osteoblasts and osteoclasts by producing paracrine signals triggered by mechanical load and assume an important role in uncoupling bone turnover [10–12]. These properties have prompted the development of strontium ranelate, a drug that has been used clinically for more than a decade in Europe, as an orally administered agent for the prevention of fractures associated with osteoporosis [10,13]. Unfortunately, its use is now strictly restricted due to clinical evidence of systemic effects including a higher incidence of cardio-vascular events [14]. This clearly points out the interest of developing bioactive strontium-containing ceramic scaffolds capable of *in situ* strontium release, thereby avoiding the systemic adverse effects of strontium ranelate. Several research groups have investigated the effect of strontium additions to bioactive glasses and glass-ceramics and demonstrated enhancement in apatite forming ability and osteoblast formation and differentiation, as well as controlled ion release [15,16], while *in vivo* studies demonstrated enhanced bone regeneration [17–20]. However, few of these studies investigated whether strontium was incorporated into newly formed bone. Our recent work investigated the thermal behavior and microstructure of fluorapatite glass-ceramics and the effect of strontium additions on their bioactivity and strontium-release ability [21,22]. It was shown that strontium additions in this glass system led to a finer microstructure, increased solubility and promoted sustained strontium release [23].

The aim of the present work was to investigate the surface microstructure, macrostructure, compressive strength and *in vivo* performance of strontium-releasing fluorapatite glass-ceramics scaffolds in the SiO_2–Al_2O_3–P_2O_5–MgO–Na_2O–K_2O–(Ca, Sr)O–CaF_2 system. The overall hypothesis was that partial replacement of strontium for calcium in the glass composition and further strontium release from the glass-ceramic scaffold would promote *in vivo* bone formation in a murine critical size calvarial defect.

2. Materials and methods

2.1. Glass preparation

Fluorapatite-based glasses in the SiO_2–Al_2O_3–P_2O_5–MgO–Na_2O–K_2O–$(Ca_{(1-x)}Sr_x)O$–CaF_2 system, with increasing amounts of strontium from 0 to 24 mol% were prepared by mixing adequate amounts of reagent grade oxides and carbonates, as previously described [23]. Glasses were labeled GSr-0, GSr-12 and GSr-24 to reflect the amount of strontium in the composition (Table 1). The glasses were twice melted at 1525 °C for 3 h in platinum crucibles and cast into cylindrical ingots that were further powdered and sieved to a particle size of 45 μm or less.

2.2. Scaffold fabrication

The well-established foam replica technique was used for the preparation of the glass scaffolds [24]. Briefly, a glass slurry was first prepared by mixing the sieved glass powder with an aqueous solution of polyvinyl alcohol (PVA) at a concentration of 0.5 wt%. A 45 ppi reticulated polyurethane foam with a pore size of about 600 μm and strut diameter of about 150 μm (Foam Mart) was chosen as sacrificial template. Scaffolds were produced by two successive immersions of polyurethane (PU) foam (Foam Mart) cylinders (12 mm in diameter, 6 mm in height) in the glass slurry. The excess slurry was removed by compression of the impregnated foams, followed by gentle blowing with compressed air. Impregnated foam cylinders were dried at room temperature for 90 min and sintered under vacuum using a previously reported Rapid Vacuum Sintering technique [25]. This technique allows burnout step and sintering step to take place successively in one rapid firing cycle. The heating rate was 55 °C per minute, the second firing was performed without vacuum. Scaffolds were sintered at 790 °C, leading to glass (GSr-0) or glass-ceramic scaffolds (GCSr-12 and GCSr-24). One group of the GSr-0 composition was further subjected to a heat treatment at 785 °C for 1 h to promote the crystallization of fluorapatite (GCSr-0). Glass-ceramic pellets of each composition were also prepared to analyze and image surface and in-depth crystalline phases.

2.3. Scaffold characterization

Scaffold macrostructural features were investigated by scanning electron microscopy (Hitachi S-4800 field emission SEM) on sintered scaffolds. Specimens were sputter-coated with gold prior to SEM examination. Mean pore diameter and strut thickness were measured on digital micrographs ($n = 4$ per group) using publicly available image analysis software (NIH Image J 1.48v [26]).

The mean density of the porous scaffolds ($\rho_{scaffold}$) was calculated from the measured mass and volume of the sintered cylinders ($n = 10$). The bulk density of the scaffold struts (ρ_{solid}) ($n = 10$) was determined by helium pycnometry (AccuPyc II 1340, Micromeritics). The porosity p of the scaffolds was calculated using the following equation:

$$p = 1 - \frac{\rho_{scaffold}}{\rho_{solid}} \quad (1)$$

The crystalline phases present after sintering were analyzed by x-ray diffraction (XRD) on powdered scaffolds. Scans were performed in the two-theta range 10–90° (40 kV; 44 mA) in Bragg-Brentano configuration (SmartLab, Rigaku Americas). Peak position was calibrated using silicon powder standard (NIST, 640d). XRD patterns were analyzed using PDXL-2 analysis software (Rigaku Corporation). Additional scans were performed in grazing incidence (GIXRD) on bulk glass-ceramic pellets to determine the nature of surface crystalline phases (omega incidence angle of 3 degrees in parallel beam optics configuration).

2.4. Compressive strength

The mean compressive strength was determined on cylindrical samples (3 mm in height, 8 mm in diameter, $n = 10$ per group) using a Universal Testing machine equipped with a 5kN load cell, at a crosshead speed of 0.5 mm/min according to ASTM D1621-10 [27]. Due to the step-wise failure mode characteristic of macroporous scaffolds, only the first five major peaks corresponding to a displacement equal or lower than 30% of the height of the specimen were averaged and used for the determination of the mean breaking load. Peaks occurring beyond this point were discarded to eliminate bias due to scaffold crumbling and densification.

2.5. In vivo bone formation in a murine critical size calvarial defect model

2.5.1. In vivo protocol—The *in vivo* response to the scaffolds was assessed using a critical size rat calvarial defect model. The experimental protocol was approved by the Institutional Animal Care and Use Committee of the University of Iowa (IACUC # 4041017). Surgery was performed under general anesthesia. The site was prepared aseptically and an incision was made along the sagittal plane of the cranium. A full thickness flap was reflected and a standardized transosseous bone defect (8 mm in diameter) was trephined at the center of the parietal bone under constant saline irrigation. Animals ($n = 10$ per group) were randomly assigned to one of the four treatment groups, namely GSr-0, GCSr-0, GCSr-12 and GCSr-24, or to a negative control group which received no graft. Intraperitoneal injections of calcein (10 mg/kg) and alizarin red (30 mg/kg) bone labels (Sigma Aldrich, St Louis, MO) were administered at 3 and 5 weeks to mark new forming bone surfaces.

2.5.2. Histological observations—Skulls were harvested, dehydrated in ascending concentrations of ethanol (from 75% to 100%) and embedded in polymethylmethacrylate (PMMA). Two sagittal sections of the central area of each defect were cut to a final

thickness of approximately 40 μm. Fluorescent labeling was observed using excitation/emission wavelengths of 488/500–550 nm (calcein, green), and 543/580–670 nm (alizarin red, red) on an epifluorescence microscope (Zeiss Axioscope-A1). The mineral apposition rate (MAR) was calculated by dividing the inter-labeling distance (ILD) between calcein green and alizarin red by the time interval between labeling periods (ILT), which was 14 days between the two consecutive biomarkers [28]. Other sections were stained with Stevenel's blue, followed by van Gieson's picrofuchsin for qualitative observation of new bone formation.

2.5.3. Micro-computed tomography (micro-CT) and x-ray microscopy evaluations—Bone formation within the defect was investigated by *in vivo* micro-computed tomography (micro-CT) under inhalation anesthesia at 4 weeks (Skyscan 1176). The scanner was operated at a voltage of 50 kV and a 500 μA current with a nominal resolution of 8.85 μm/pixel. In addition, *ex-vivo* analyses were also performed after sacrifice at 8 weeks using the above-listed conditions.

To provide higher resolution images and improve the rendering of the bone-scaffold interface, hemi-sectioned epoxy-embedded skulls were scanned by high resolution 3D x-ray microscopy (Zeiss Xradia 520 Versa) at 80 kV, 7W, and 0.4× magnification with no additional filter. 1601 projections were acquired with an exposure time of 2 s per projection. Dynamic ring removal software was enabled, and secondary references were collected to reduce ring artifacts. Images were reconstructed using the Xradia's reconstruction software, with down sampling of 1, beam hardening correction of 0.5, and a final reconstructed image pixel size of 8.5 μm. Images were visualized using ORS Visual SI Version 1.8.0 (ORS, Montreal, Canada).

2.5.4. SEM and energy dispersive x-ray fluorescence spectrometry of skull sections—Skull sections were polished to a 1 μm finish prior to SEM examination. Energy dispersive x-ray fluorescence spectroscopy qualitative analyses were performed on both scaffold strut sections and newly formed bone to assess elemental diffusion.

2.6. Statistical analyses

Results were analyzed by ANOVA and Tukey's test to detect statistically significant differences between groups. A p-value of less than 0.05 was considered statistically significant.

3. Results

3.1. Scaffold characterization

As mentioned earlier, the crystallization behavior, density and solubility of these glass compositions were recently reported [23]. The focus of the present manuscript was to assess the suitability of strontium-releasing compositions for producing synthetic scaffolds for bone graft substitutes.

3.1.1. Macrostructure—Scanning electron micrographs showing the macrostructure of the scaffolds are displayed in Fig. 1 (A through D). The results from pore size, strut diameter

and porosity measurements are listed in Table 2. The amount of porosity increased with strontium content in the composition, while there were no significant differences in mean pore diameter. There were no significant differences in macrostructural characteristics between the strontium free glass scaffolds (GSr-0) (Fig. 1A) and strontium-free glass-ceramic scaffolds (GCSr-0) (Fig. 1B).

3.1.2. Microstructure—Higher magnification images showing the surface microstructure are displayed in Fig. 1 (E through H). The in-depth microstructure of corresponding pellets after polishing and etching with diluted aqueous solution of hydrofluoric acid is shown in Fig. 1 (I through L). The strontium-free glass scaffold surface (GSr-0) was characterized by the presence of submicrometer flower-shaped fluorapatite crystals, about 500 nm in diameter (arrow), as previously described for this composition (Fig. 1E) [21,22,29].). As expected for a glass, the corresponding in-depth microstructure was featureless (Fig. 1I). The strontium-free glass-ceramic scaffold surface (GCSr-0; Fig. 1F) was characterized by the presence of cuboid crystals, about 150 nm in size (arrow), resting on a primary microstructure consisting of densely packed flower-shaped fluorapatite crystals, about 1 μm in diameter (Fig. 1J). Strontium-containing glass-ceramic scaffolds (GCSr-12; Fig. 1G and GCSr-24; Fig. 1H) exhibited a generally smooth surface with only a few dispersed submicrometer platelets of hexagonal shape (arrows). These platelets were approximately 100 nm in diameter for GCSr-12 and about half that size for GCSr-24. The underlying microstructure consisted of sparse Sr-substituted flower-shaped crystals, about 0.8 μm in diameter, for GCSr-12, (Fig. 1K) and densely packed Sr-fluorapatite flower-shaped crystals (about 0.5 μm in diameter) for GCSr-24 (Fig. 1L).

3.1.3. Crystalline phases—Results from x-ray powder diffraction analyzes are displayed in Fig. 2 (A–D). The amount of crystallization increased with the amount of strontium in the glass composition. Traces of fluorapatite (PDF 15-876) were found in the as-sintered strontium-free scaffolds (GSr-0), while fully crystallized fluorapatite was present after crystallization heat treatment (GCSr-0). Strontium-substituted fluorapatite crystallized in the strontium-containing glasses, in agreement with our previous work [23]. The extent of strontium substitution in the fluorapatite structure was in line with the amount of strontium in the glass composition [23,30–32].

Grazing incidence x-ray diffraction patterns of glass and glass-ceramic pellets are shown in Fig. 3. Surface crystallization of fluorapatite was observed for the strontium-free glass pellet (GSr-0; Fig. 3A). Akermanite ($CaMg_2Si_2O_7$) crystallized in addition to fluorapatite for the strontium-free glass-ceramic (GCSr-0; Fig. 3B). Only strontium-substituted fluorapatite was found for GCSr-12 (Fig. 3C) and GCSr-24 (Fig. 3D).

3.1.4. Compressive strength—The mean compressive strength for the various groups is summarized in Table 2. Scaffolds produced from the strontium-free composition, whether in the as-sintered stage (GSr-0) or after heat treatment (GCSr-0), exhibited significantly higher mean compressive strength than all other groups. The mean compressive strength of the strontium-containing groups decreased with the amount of strontium in the composition but differences between these two groups were not statistically significant ($p > 0.05$).

3.2. In vivo study

3.2.1. Histological observations—Representative histological sections stained with Stevenel's blue-van Gieson picrofuschin are shown in Fig. 4 (A5 through E5).

The amount of new bone formed at 8 weeks (n = 5 per group) is reported in Table 2. The strontium-free glass-ceramic group GCSr-0 had the highest amount of new bone formed (Fig. 4A5), followed by group GCSr-24 (Fig. 4C5) and GCSr-12 (Fig. 4B5). Group GSr-0 had the lowest amount of new bone formation (Fig. 4D5). However, due to the high variability observed with groups GCSr-12 and GCSr-24, there were no statistically significant differences between groups ($p > 0.05$).

3.2.2. Mineral apposition rate—Histological sections showing new bone formation after bone labeling with calcein and alizarin red fluorochromes, with corresponding merged images and bright field images, are shown in Fig. 4 (A1 through E1, A2 through E2, A3 through E3 and A4 through E4, respectively). The inter-labeling distance was calculated by measuring the area stained in green and associated radius, followed by the area stained in red and associated radius. The mean inter-labeling distance was obtained from the difference between the two radii. The mineral apposition rate (MAR, n = 8 per group) was calculated by dividing the inter-labeling distance between calcein green and alizarin red labels by the time interval between fluorochrome injections, which was 14 days [33]. Results are summarized in Table 2. A representative micrograph at higher magnification, showing both fluorochromes for GCSr-24 is shown in Fig. 5.

The mean MAR between weeks 3 and 5 was 2.3 ± 0.4 μm/day for the negative control group, which was not statistically different from group GSr-0. The mean MAR for group GCSr-24 (9.2 ± 3.7 μm/day) was significantly higher than that of the control group or GSr-0, but not significantly different from that of the other groups ($p > 0.05$). Although relating only three data points, the relationship between strontium content and MAR was linear (R^2=0.968).

3.3. Ex-vivo micro-CT X-ray analyses

Representative 3D images of hemi-sectioned scaffolds and corresponding 2D projections are displayed in Fig. 6.

The amount of new bone formation was significantly higher for GCSr-0, followed by GCSr-24, which was not significantly different from GCSr-12 or GSr-0. Results are summarized in Table 2.

3.4. SEM and energy dispersive X-Ray fluorescence (XRF) analyses of skulls sections

Results from semi-quantitative energy dispersive XRF analyses of skull sections after 8 weeks *in vivo* are shown in Fig. 7 (A through D). Mean relative proportions of the main elements found are displayed for at least eight point analyses on both newly formed bone and scaffold material for each group. A representative skull cross section is shown in Fig. 7E. Higher magnification is shown in Fig. 7F, arrows indicate dissolution zone around scaffold struts. It is interesting to note that a significant amount of fluorine, together with

smaller amounts of aluminum and magnesium were found in newly formed bone, regardless of composition. Of interest, small amounts of strontium (1–2 at%) were also present in newly formed bone for GCSr-12 and GCSr-24.

4. Discussion

The amount of interconnected porosity and pore size observed in all groups fit the established criteria for bone graft substitutes. These characteristics, specifically pore interconnectivity, are paramount for successful angiogenesis and osteoconduction throughout the scaffold structure, by allowing free permeation and nutrient circulation.

SEM characterization revealed that the strontium-free scaffolds, whether as-sintered or heat treated, were adequately sintered, with homogeneous strut surface, while groups GCSr-12 and GCSr-24 exhibited a more granular appearance, with coalesced rounded particles, indicative of less complete sintering. This can be explained by the effect of strontium on the thermal behavior of glass-ceramics in this system, lowering the crystallization temperature and narrowing the temperature window for adequate sintering. The lower degree of sintering led to a greater amount of porosity and larger pore size, as sintering is associated with dimensional shrinkage. Crystallization was confirmed by XRD analyses, showing a significant amount of Sr-fluorapatite in groups GCSr-12 and GCSr-24. The lower degree of sintering of these compositions is likely responsible for the significantly lower mean compressive strength, compared to the strontium-free groups. The slightly higher mean compressive strength of the strontium-free glass ceramic group (GCSr-0; 1.72 ± 0.61 MPa) compared to the strontium-free glass group (GSr-0; 1.52 ± 0.55 MPa) reflects the effect of crystalline reinforcement provided by the core crystallization of fluorapatite. However, compressive strength values all reflect the mechanical integrity of the scaffolds, which is adequate for use in non-load-bearing situations.

New bone formation was significantly higher for group GCSr-0, followed by GCSr-24, GCSr-12 and GSr-0. These results point out the importance of surface microstructure in osseointegration processes. It is well established that implant surfaces are a critical factor determining local tissue response immediately after implantation, as well as endosseous healing [34,35]. The present study revealed a significantly higher bone formation associated with glass-ceramic scaffolds (GCSr-0) compared to glass scaffolds (GSr-0) of same chemical composition and similar macrostructure, including pore size and porosity as well as comparable compressive strength. It is important to note that the only difference between these two groups was the presence of akermanite crystals ($Ca_2MgSi_2O_7$) in the submicrometer range at the surface of the struts (Fig. 1F), thereby in direct contact with the surrounding tissues. GIXRD confirmed surface crystallization of akermanite (Fig. 3B). We hypothesize that this type of microstructure is highly efficient in promoting contact osteogenesis, providing crystalline anchors with a topography reminiscent of a cement line at both the micro and nanoscale, thereby triggering osteoblastic activity. Conversely, akermanite glass-ceramics have been shown to be bioactive and promote osteogenesis [36,37].

The mineral apposition rate (MAR) was highest for the GCSr-24 group (9.2 ± 3.7 μm/day), while there were no differences between the other groups and the negative control group. This confirms the efficacy of strontium in promoting osteoblastic activity. Our previous work showed sustained release of strontium from these compositions [23]. Although group GCSr-12 was associated with the second highest MAR (6.9 ± 2.3 μm/day), the amount of strontium released may not have been sufficient to lead to a significant difference from the negative control group. The mean MAR value obtained for the strontium-free glass (5.7 ± 2.2 μm/day) and glass-ceramic (6.3 ± 2.2 μm/day) compare well with previously published data in the literature, for calcium-phosphate-based silicate ceramics (5–6 μm/day) [38].

The results from standard micro-CT and high-resolution x-ray microscopy (XRM) confirm findings from histomorphometric analyzes, with new bone formation extending to the center of the scaffolds for all experimental groups and highest new bone formation for GCSr-0 and GCSr-24. Both optical and 3D x-ray microscopy also revealed the presence of a zone of darker contrast and lower radiographic density forming the outer shell of the scaffold struts, regardless of chemical composition (Fig. 6B through E and Fig. 7F). This zone is tentatively identified as a reaction zone indicative of scaffold biodegradation and interaction with surrounding cells and nutrients. This finding was expected, as we already reported the bioactivity of these compositions, and their solubility in TRIS-HCl at pH 7.4, together with sustained strontium release for relevant compositions [23]. The release of strontium from the scaffolds for groups GCSr-12 and GCSr-24 was indirectly confirmed by its identification by x-ray fluorescence spectrometry within newly formed bone for these compositions (Fig. 7C and 7D). The incorporation of fluoride into newly formed bone is in line with previous studies showing that fluoride is readily incorporated into bone when available during bone formation [39,40]. Although present in the glass compositions in modest amount (0.8 mol %), aluminum was also found in newly formed bone. This is not desirable as aluminum has been shown to have negative effects on osteoblastic activity. However, we postulate that aluminum-free glass compositions would possess very similar chemical and physical properties due to the small amount involved.

5. Conclusion

In situ delivery of key elements is an attractive route to promote both angiogenesis and osteogenesis. We first demonstrated sustained *in vitro* release of strontium from fluorapatite-based glass compositions, the present work shows evidence of *in vivo* release leading to a higher mineral apposition rate compared to undoped compositions.

The second important finding from this study is that both surface microstructure and chemistry also played a key role in promoting new bone formation. The presence of magnesium and silicon-rich akermanite crystals at the undoped glass-ceramic scaffold surface was associated with higher *in vivo* bone formation compared to the corresponding glass scaffold surface.

Acknowledgments

This work was supported by the National Institutes of Health, National Institute of Dental Research (Grant number R01-DE19972).

The use of the x-ray microscope (Xradia Versa 520) was supported in part by Shared Instrumentation Grant 1S10OD018503-01 from the National Institutes of Health.

References

1. Denry I, Kuhn LT. Design and characterization of calcium phosphate ceramic scaffolds for bone tissue engineering. Dent. Mater. 2016; 32(1):43–53. [PubMed: 26423007]
2. Bose S, Roy M, Bandyopadhyay A. Recent advances in bone tissue engineering scaffolds. Trends Biotechnol. 2012; 30(10):546–554. [PubMed: 22939815]
3. Hench L. Bioactive glasses and glass-ceramics. In: Shackelford J, editorBioceramics. Trans Tech Publications; Baudrain: 1999. 37–64.
4. Hench L, Splinter R, Allen W, Greenlee T. Bonding mechanisms at the interface of ceramic prosthetic materials. J. Biomed. Mater. Res. 1971; 5(6):117–141.
5. Chen QZZ, Thompson ID, Boccaccini AR. 45S5 Bioglass (R)-derived glass-ceramic scaffolds for bone tissue engineering. Biomaterials. 2006; 27(11):2414–2425. [PubMed: 16336997]
6. Groh D, Dohler F, Brauer DS. Bioactive glasses with improved processing. Part 1. Thermal properties, ion release and apatite formation. Acta Biomater. 2014; 10(10):4465–4473. [PubMed: 24880003]
7. Bose S, Fielding G, Tarafder S, Bandyopadhyay A. Understanding of dopant-induced osteogenesis and angiogenesis in calcium phosphate ceramics. Trends Biotechnol. 2013; 31(10):594–605. [PubMed: 24012308]
8. LeGeros RZ. Properties of osteoconductive biomaterials: calcium phosphates. Clin. Orthopaedics Related Res. 2002; 395:81–98.
9. Atkins GJ, Welldon KJ, Halbout P, Findlay DM. Strontium ranelate treatment of human primary osteoblasts promotes an osteocyte-like phenotype while eliciting an osteoprotegerin response. Osteoporos int. 2009; 20(4):653–654. [PubMed: 18763010]
10. Cianferotti L, D'Asta F, Brandi ML. A review on strontium ranelate long-term antifracture efficacy in the treatment of postmenopausal osteoporosis. Ther. Adv. Musculoskeletal Dis. 2013; 5(3):127–139.
11. Tan S, Zhang B, Zhu X, Ao P, Guo H, Yi W, Zhou G-Q. Deregulation of bone forming cells in bone diseases and anabolic effects of strontium-containing agents and biomaterials. Biomed Res. Int. 2014; 2014:12.
12. Bakker AD, Zandieh-Doulabi B, Klein-Nulend J. Strontium Ranelate affects signaling from mechanically-stimulated osteocytes towards osteoclasts and osteoblasts. Bone. 2013; 53(1):112–119. [PubMed: 23234812]
13. Blake GM, Fogelman I. Strontium ranelate: a novel treatment for postmenopausal osteoporosis: a review of safety and efficacy. Clin. Int. Aging. 2006; 1(4):367–375.
14. Donneau AF, Reginster JY. Cardiovascular safety of strontium ranelate: real-life assessment in clinical practice. Osteoporosis Int. 2014; 25(2):397–398.
15. Zhang JH, Zhao SC, Zhu YF, Huang YJ, Zhu M, Tao CL, Zhang CQ. Three-dimensional printing of strontium-containing mesoporous bioactive glass scaffolds for bone regeneration. Acta Biomater. 2014; 10(5):2269–2281. [PubMed: 24412143]
16. Zhu YF, Zhu M, He X, Zhang JH, Tao CL. Substitutions of strontium in mesoporous calcium silicate and their physicochemical and biological properties. Acta Biomater. 2013; 9(5):6723–6731. [PubMed: 23376133]
17. Grynpas MD, Hamilton E, Cheung R, Tsouderos Y, Deloffre P, Hott M, Marie PJ. Strontium increases vertebral bone volume in rats at a low dose that does not induce detectable mineralization defect. Bone. 1996; 18(3):253–259. [PubMed: 8703581]
18. Lin KL, Xia LG, Li HY, Jiang XQ, Pan HB, Xu YJ, Lu WW, Zhang ZY, Chang J. Enhanced osteoporotic bone regeneration by strontium-substituted calcium silicate bioactive ceramics. Biomaterials. 2013; 34(38):10028–10042. [PubMed: 24095251]
19. Xie HX, Wang JY, Li CS, Gu ZP, Chen QM, Li LJ. Application of strontium doped calcium polyphosphate bioceramic as scaffolds for bone tissue engineering. Ceram. Int. 2013; 39(8):8945–8954.

20. Zreiqat H, Ramaswamy Y, Wu C, Paschalidis A, Lu Z, James B, Birke O, McDonald M, Little D, Dunstan CR. The incorporation of strontium and zinc into a calcium-silicon ceramic for bone tissue engineering. Biomaterials. 2010; 31(12):3175–3184. [PubMed: 20117832]
21. Denry I, Holloway JA. Fluorapatite Glass-Ceramics US Patent Number. 9,125,967. 2015.
22. Denry I, Holloway JA. Low temperature sintering of fluorapatite glass-ceramics. Dent. Mater. 2014; 30(2):112–121. [PubMed: 24252652]
23. Denry I, Goudouri O-M, Harless J, Hubbard E, Holloway J. Strontium-releasing fluorapatite glass-ceramics: Crystallization behavior, microstructure, and solubility. J. Biomed Mater. Res. Part B. 2018; 106(4):1421–1430.
24. Schwartzwalder K, Somers AV. Method of Making Porous Ceramic Articles. General Motors Corporation; United States: 1963.
25. Denry I, Goudouri OM, Harless J, Holloway JA. Rapid vacuum sintering: A novel technique for fabricating fluorapatite ceramic scaffolds for bone tissue engineering. J. Biomed. Mater. Res. Part B-Appl. Biomater. 2018; 106(1):291–299. [PubMed: 28135032]
26. Schneider CA, Rasband WS, Eliceiri KW. NIH Image to ImageJ: 25 years of image analysis. Nat. Methods. 2012; 9(7):671–675. [PubMed: 22930834]
27. ASTM, D1621-10, Standard Test Method for Compressive Properties Of Rigid Cellular Plastics. ASTM International; West Conshohocken, PA: 2010.
28. Dempster DW, Compston JE, Drezner MK, Glorieux FH, Kanis JA, Malluche H, Meunier PJ, Ott SM, Recker RR, Parfitt AM. Standardized nomenclature, symbols, and units for bone histomorphometry: a 2012 update of the report of the asbmr histomorphometry nomenclature committee. J. Bone Miner. Res. 2013; 28(1):2–17. [PubMed: 23197339]
29. Denry I, Holloway JA, Gupta PK. Effect of crystallization heat treatment on the microstructure of niobium-doped fluorapatite glass-ceramics. J. Biomed. Mater. Res. Part B-Appl. Biomater. 2012; 100B(5):1198–1205.
30. Bigi A, Falini G, Gazzano M, Roveri N, Tedesco E. Structural refinements of strontium substituted hydroxylapatites. Mater. Sci. Forum. 1998:814–819.
31. Michie EM, Grimes RW, Fong SK, Metcalfe BL. Predicted energies and structures associated with the mixed calcium strontium fluorapatites. J. Solid State Chem. 2008; 181(12):3287–3293.
32. Rakovan JF, Hughes JM. Strontium in the apatite structure: strontian fluorapatite and belovite-(Ce). Can. Mineral. 2000; 38:839–845.
33. Parfitt AM, Drezner MK, Glorieux FH, Kanis JA, Malluche H, Meunier PJ, Ott SM, Recker RR. Bone histomorphometry – standardization of nomenclature, symbols, and units. J. Bone Miner. Res. 1987; 2(6):595–610. [PubMed: 3455637]
34. Davies JE. Understanding peri-implant endosseous healing. J. Dent. Educ. 2005; 67(8):932–949.
35. Davies JE. Bone bonding at natural and biomaterial surfaces. Biomaterials. 2007; 28(34):5058–5067. [PubMed: 17697711]
36. Xia LG, Yin ZL, Mao LX, Wang XH, Liu JQ, Jiang XQ, Zhang ZY, Lin KL, Chang J, Fang B. Akermanite bioceramics promote osteogenesis, angiogenesis and suppress osteoclastogenesis for osteoporotic bone regeneration. Sci. Rep. 2016; 6:17. [PubMed: 28442711]
37. Wu C, Zhou Y, Lin C, Chang J, Xiao Y. Strontium-containing mesoporous bioactive glass scaffolds with improved osteogenic/cementogenic differentiation of periodontal ligament cells for periodontal tissue engineering. Acta Biomater. 2012; 8(10):3805–3815. [PubMed: 22750735]
38. Hing KA, Wilson LE, Buckland T. Comparative performance of three ceramic bone graft substitutes. Spine J. 2007; 7(4):475–490. [PubMed: 17630146]
39. Chachra D, Turner CH, Dunipace AJ, Grynpas MD. The effect of fluoride treatment on bone mineral in rabbits. Calcified Tissue Int. 1999; 64(4):345–351.
40. Mousny M, Omelon S, Wise L, Everett ET, Dumitriu M, Holmyard DP, Banse X, Devogelaer JP, Grynpas MD. Fluoride effects on bone formation and mineralization are influenced by genetics. Bone. 2008; 43(6):1067–1074. [PubMed: 18755305]

Statement of Significance

The present work demonstrates the *in vivo* action of strontium-containing glass-ceramic scaffolds. These bone graft substitutes are targeted at non load-bearing bone defects. Results show that strontium is successfully incorporated in newly formed bone. This is associated with a significantly higher Mineral Apposition Rate. The benefits of *in situ* release of strontium are demonstrated. The broader scientific impact of this works builds on the concept of resorbable ceramic scaffolds as reservoirs of ionic species capable of enhancing bone regeneration.

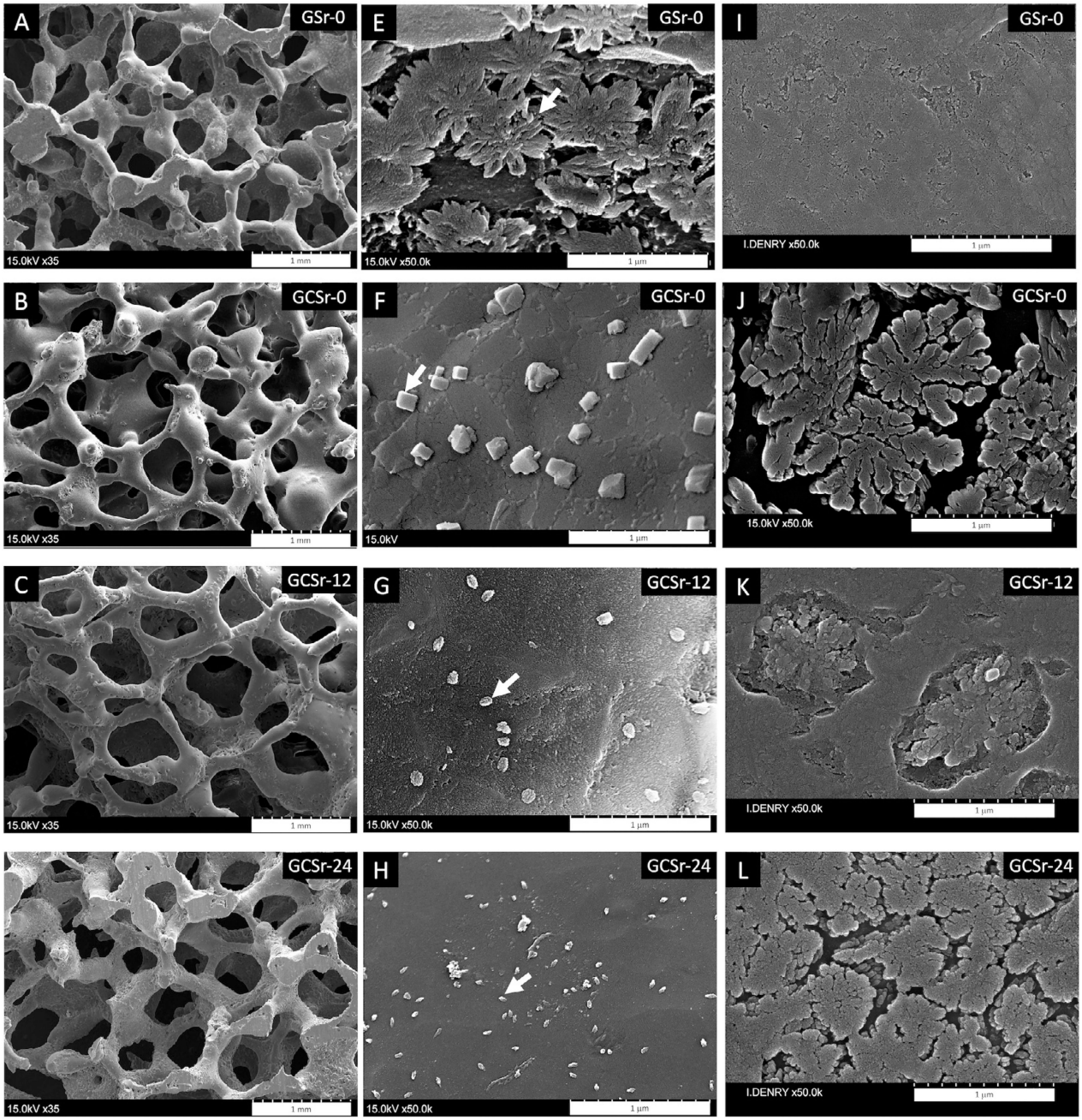

Fig. 1.

Scanning electron micrographs of various scaffolds. A and E: GSr-0, arrow indicates fluorapatite crystal; B and F: GCSr-0, arrow indicates akermanite crystal; C and G: GCSr-12, arrow indicates Sr-fluorapatite platelet; D and H: GCSr-24, arrow indicates Sr-fluorapatite platelet; I through L: scanning electron micrographs of polished and etched specimens showing underlying microstructure (I: GSr-0; J: GCSr-0; K: GCSr-12; L: GCSr-24).

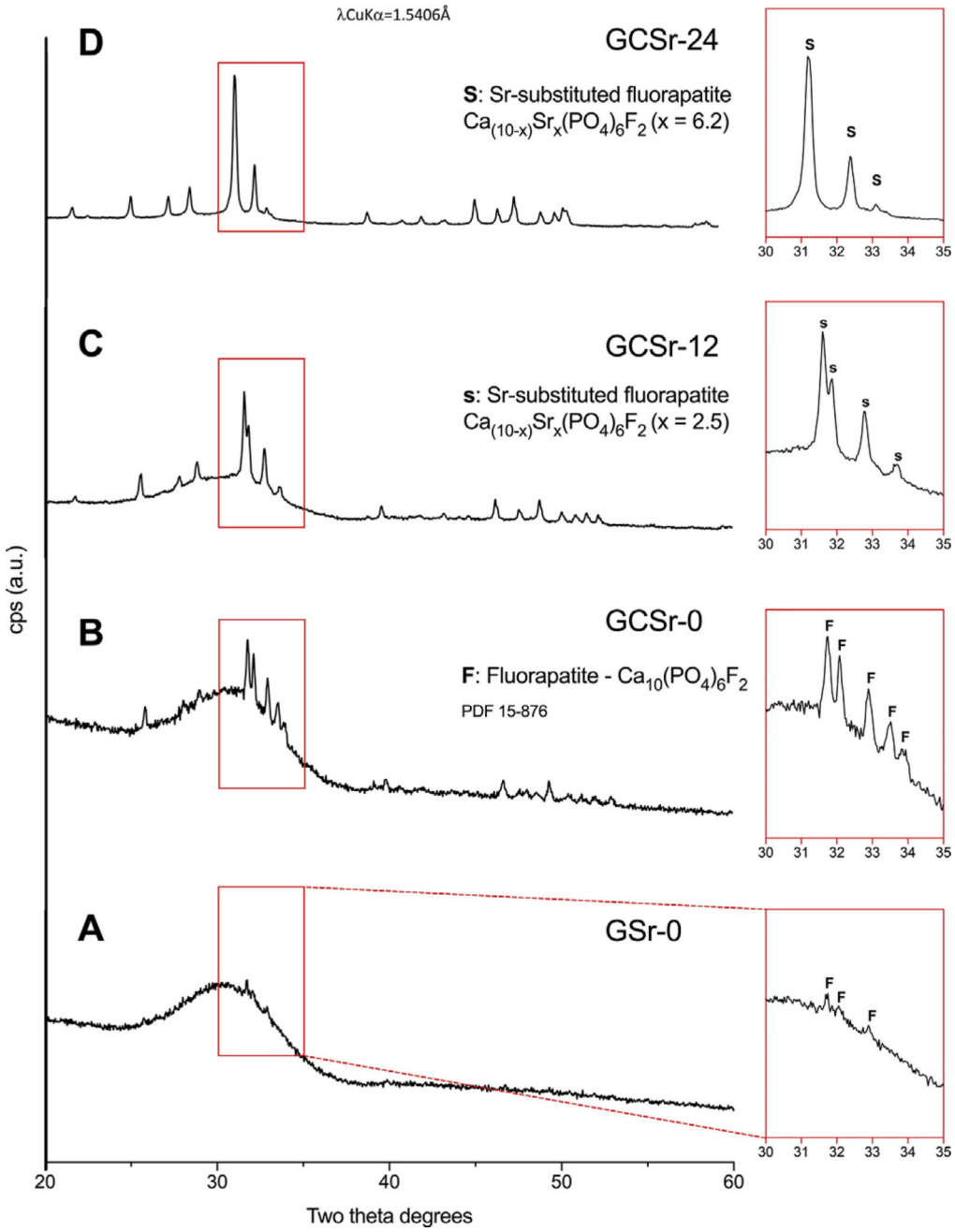

Fig. 2.

X-ray diffraction patterns of powdered scaffolds (A: GSr-0; B: GCSr-0; C: GCSr-12; D: GCSr-24).

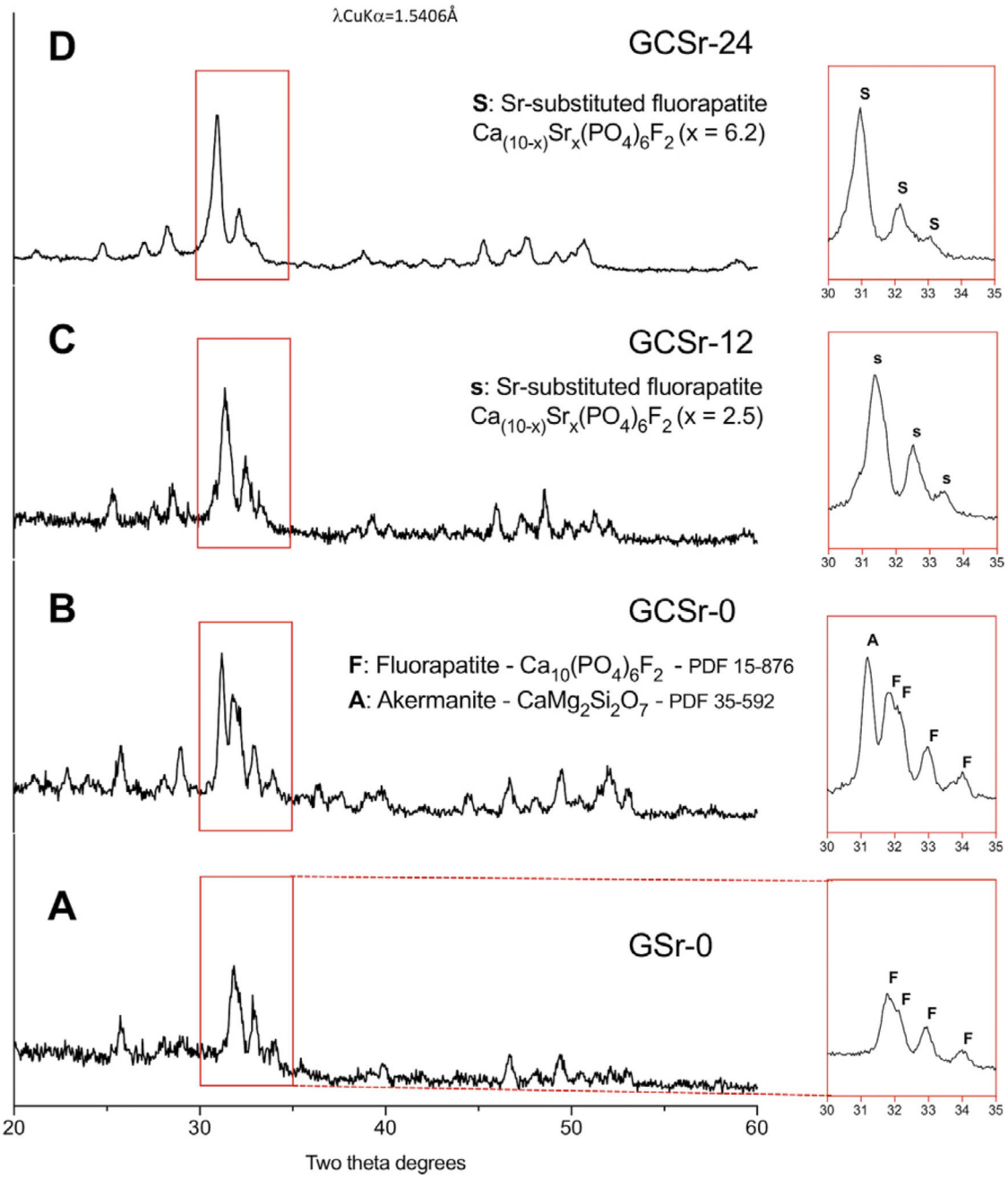

Fig. 3.

Grazing incidence x-ray diffraction patterns of sintered glass and glass-ceramic pellet surfaces (A: GSr-0; B: GCSr-0; C: GCSr-12; D: GCSr-24).

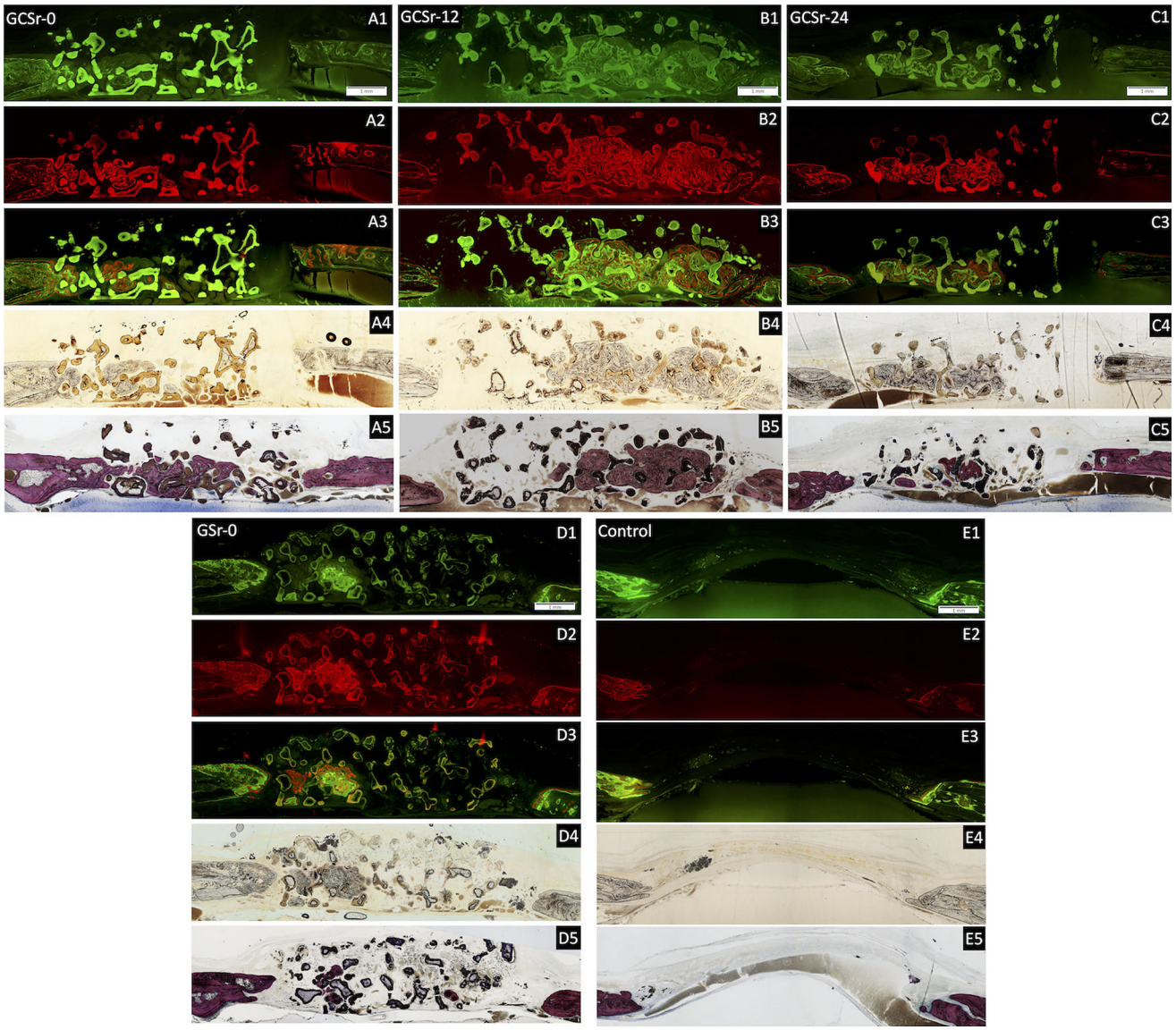

Fig. 4.

Representative histological skull sections. A1 through E1: calcein label; A2 through E2: alizarin red label; A3 through E3: combined labeling; A4 through E4: bright field image; A5 through E5: Stevenel's blue-van Gieson picrofuschin staining. (Bar: 1 mm).

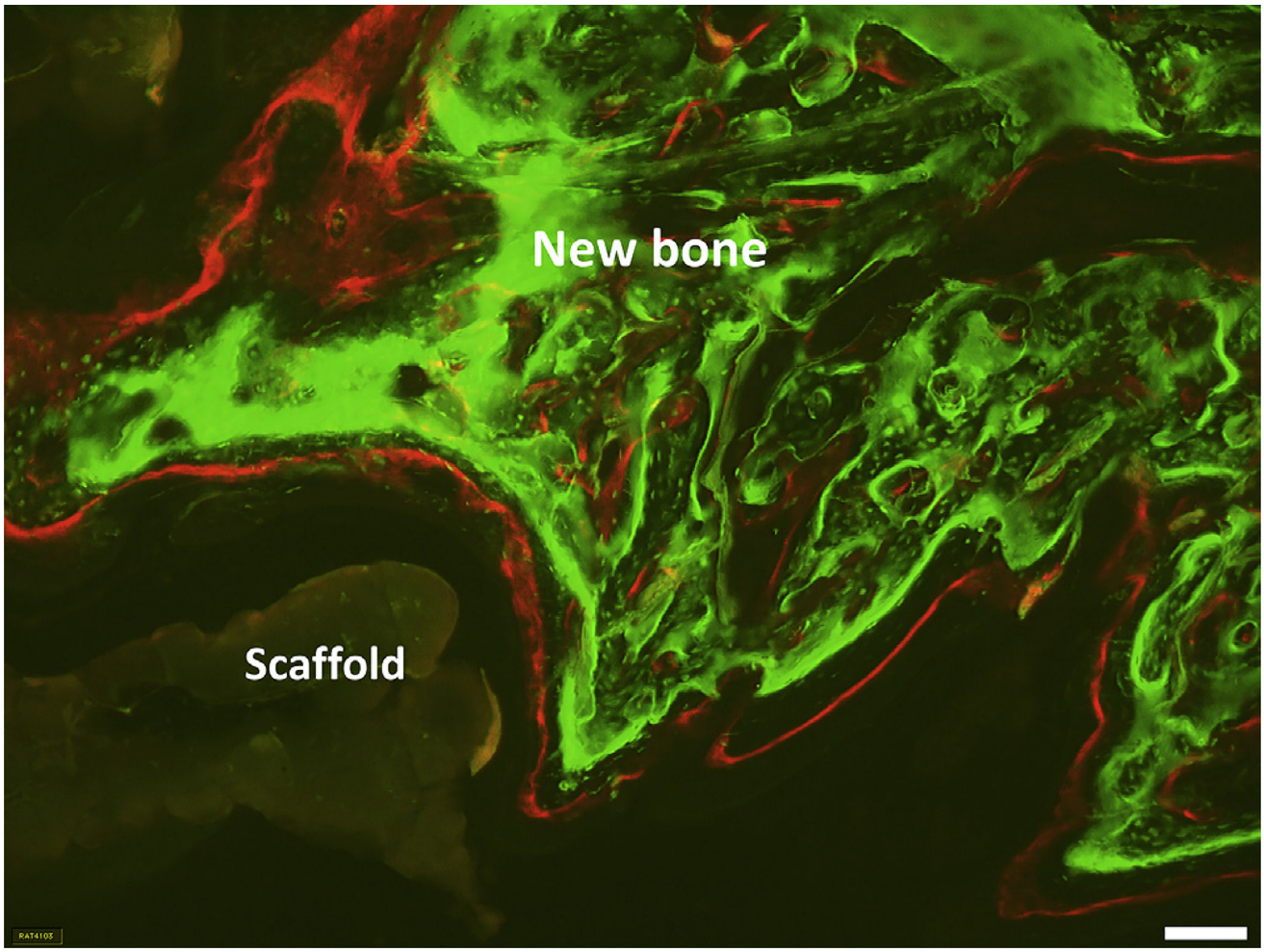

Fig. 5.
Representative micrograph of histological skull section showing both fluorochromes labels for GCSr-24. (bar: 100 μm).

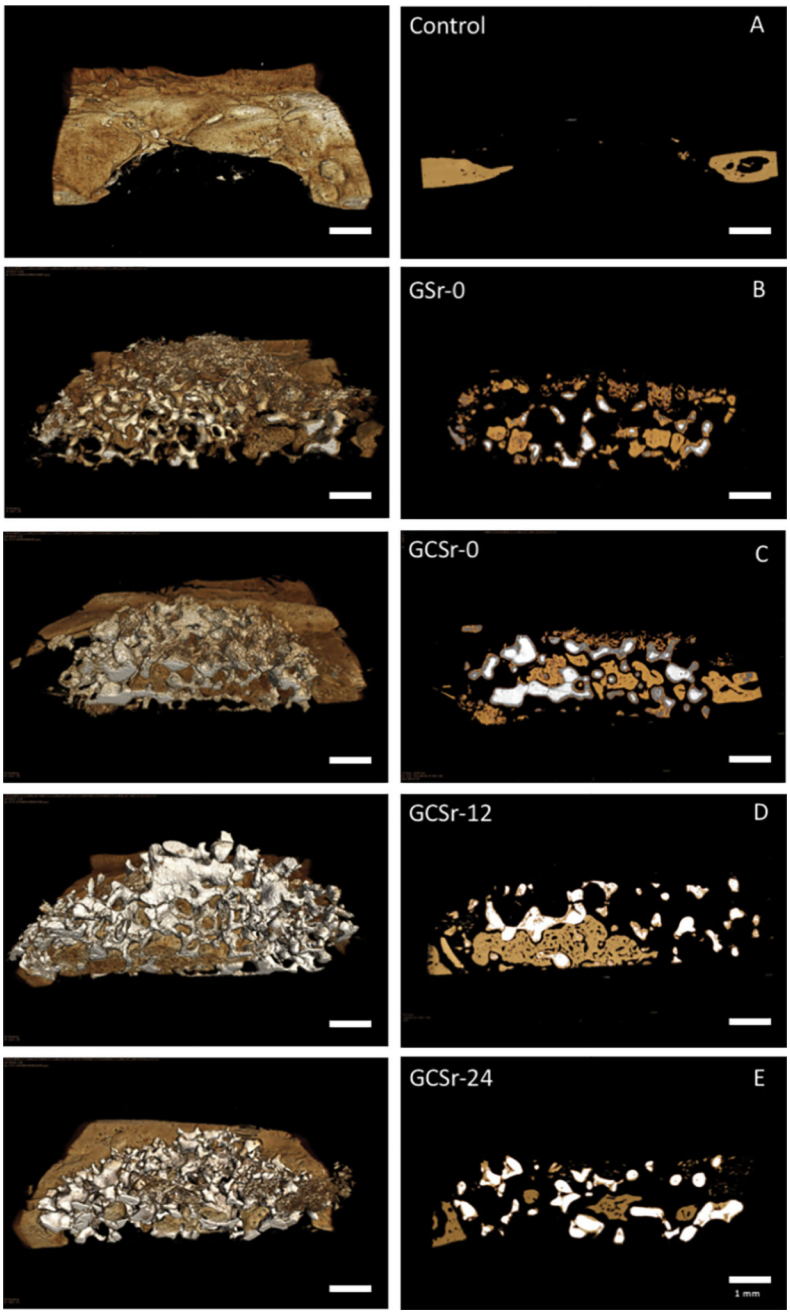

Fig. 6.

Representative 3D (left) and 2D (right) x-ray microscopy images of hemisectioned scaffolds after 8 weeks *in vivo*. A: negative control; B: GSr-0; C: GCSr-0; D: GCSr-12; E: GCSr-24.

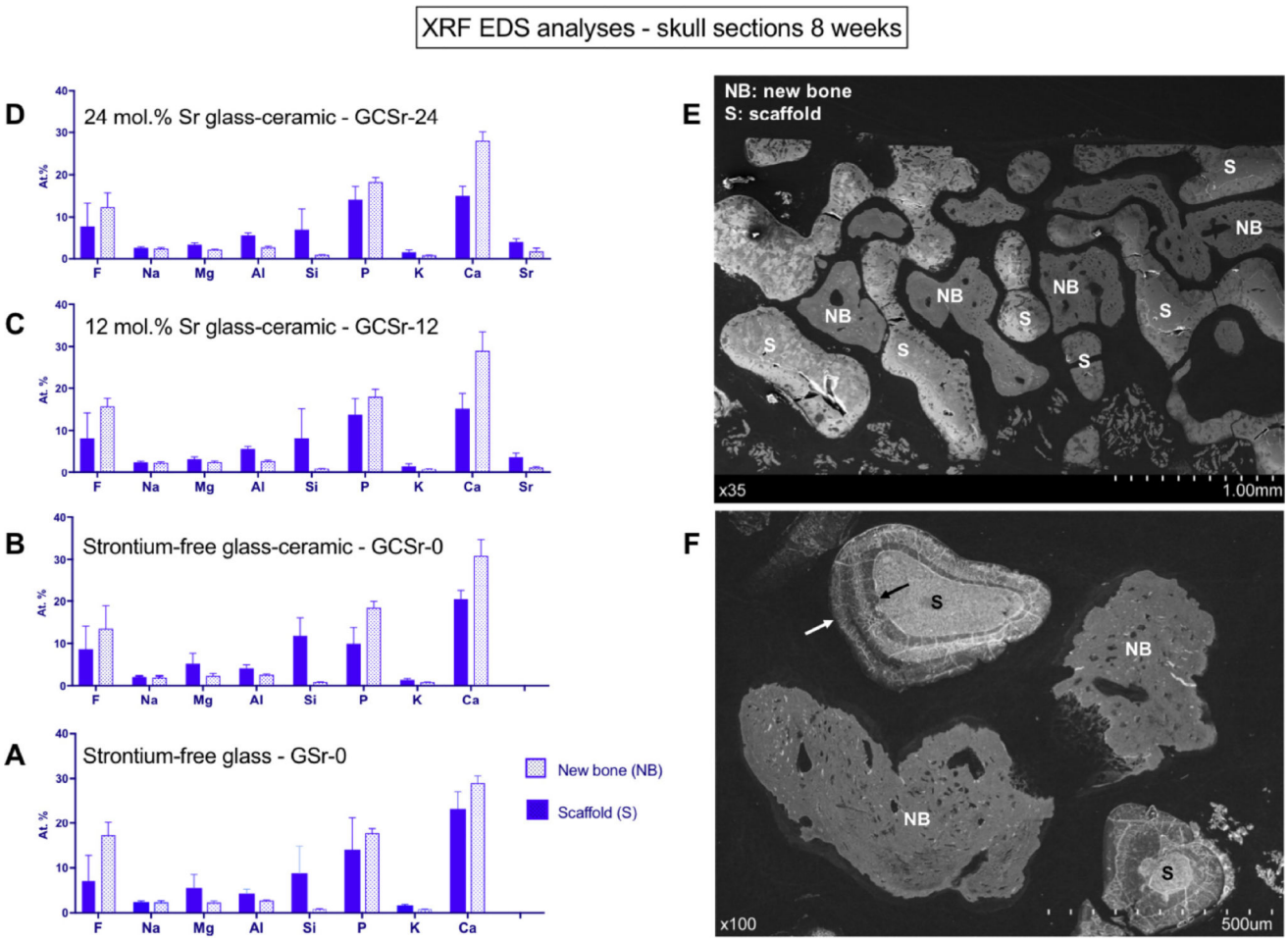

Fig. 7.

Summary of EDS XRF analyses of skull sections at 8 weeks. A: GSr-0; B: GCSr-0; C: GCSr-12; D: GCSr-24; E: representative skull section showing scaffold (S) and new bone (NB); F: higher magnification showing glass-ceramic scaffold strut surrounded by biodegradation zone (arrows).

Table 1

Chemical composition of the glasses prepared (mol%).

	GSr-0	GSr-12	GSr-24
SiO_2	31.5	31.5	31.5
MgO	21.2	21.2	21.2
Nb_2O_5	0.2	0.2	0.2
CaO	24.0	12.0	0.0
SrO	**0.0**	**12.0**	**24.0**
Na_2O	2.3	2.3	2.3
K_2O	3.8	3.8	3.8
Al_2O_3	0.8	0.8	0.8
CaF_2	11.2	11.2	11.2
P_2O_5	5.0	5.0	5.0

Table 2

Architectural characteristics, mean compressive strength and *in vivo* response for the various experimental groups (NA: not applicable).

Group	GSr-0	GCSr-0	GCSr-12	GCSr-24	Control
Strut diameter (μm)	187 ± 52[a]	192 ± 26[a]	281 ± 45[b]	263 ± 77[b]	NA
Pore diameter (μm)	496 ± 133[a]	502 ± 92[a]	551 ± 116[a]	540 ± 144[a]	NA
Strut density (g/cm^3)	2.927 ± 0.008	2.923 ± 0.017	3.188 ± 0.005	3.353 ± 0.021	NA
Porosity (%) – (SEM)	73.4 ± 3.8[a]	76.1 ± 2.9[ab]	79.1 ± 3.3[b]	85.3 ± 1.2[c]	NA
Porosity (%) – (micro-CT)	61.8 ± 7.5[a]	66.9 ± 6.1[ab]	74.6 ± 0.6[bc]	80.5 ± 2.0[c]	NA
Compressive strength (MPa)	1.52 ± 0.55[a]	1.72 ± 0.61[a]	0.83 ± 0.37[b]	0.32 ± 0.06[b]	NA
Mineral Apposition Rate (μm/day)	5.7 ± 2.2[ab]	6.3 ± 2.2[bc]	6.9 ± 2.3[bc]	9.2 ± 3.7[c]	2.3 ± 0.4[a]
New bone formation (%) (2D histological sections)	10.7 ± 5.9[a]	22.3 ± 6.7[a]	20.3 ± 12.6[a]	22.0 ± 15.7[a]	NA
Percent bone volume BV/TV (%) (mirco-CT)	23.4 ± 4.5[b]	38.5 ± 10.9[c]	24.8 ± 7.1[b]	32.5 ± 7.2[bc]	3.5 ± 2.3[a]

[*] Identical letters denote not statistically significant differences ($p > 0.05$).